A highly active CH_4 catalyst correlated with solid oxide fuel cell anode performance

Yuanhui Su[1], Tao Wei[1,*], Yining Li[1], Baoyi Yin[1], Yu Huan[1]*, Dehua Dong[1], Xun Hu[1], and Bolong Huang[2,*]

[1]School of Material Science and Engineering, University of Jinan, Jinan 250022, China
[2]Department of Applied Biology and Chemical Technology, The Hong Kong Polytechnic University, Hung Hom, Kowloon, Hong Kong SAR, China

* Correspondence: mse_weit @ujn.edu.cn; mse_huany @ujn.edu.cn; bhuang@polyu.edu.hk

Abstract: Methane catalytic abilities are considered to be an important and direct form of experimental evidence for evaluating the efficacy of mixed oxide-ion/electron conductors (MIEC) as anode materials for solid oxide fuel cells (SOFCs) with CH_4 as the fuel gas. Therefore, a direct link between the quantifiable methane-conversion abilities and CH_4-based SOFC electrochemical performance is urgently needed. Here, H_2-reduced Sr_2ZnMoO_6 (R-SZMO) as an anode example exhibits excellent catalytic abilities and tolerance to coking when using CH_4 as the fuel gas, which is dominated by the formation of intrinsic anion-Frenkel defect pairs. DFT calculations reveal that the efficient electron transfer process and optimal selectivity towards CH_4 conversion are both on the R-SZMO (110) surface. Therefore, applying high CH_4 activity R-SZMO as the anode catalyst gives excellent anti-carbon deposition performance, high power output, and long-term stability for SOFCs with CH_4 as the fuel gas.

Keywords: SOFCs anode; anode oxygen permeability; CH_4 conversion rate; Sr_2ZnMoO_6;

1. Introduction

SOFCs as highly efficient energy conversion and controlling devices, the functions of its electrode materials not only promote the fuel-gas catalytic reaction, but also ensure the fast transportation of electrons between electrode and external circuit, and ions between electrode and electrolyte. In the pursuit of better electrode materials, researchers poured more and more interest in analyzing the transporting mechanism, transport mode and transport capacity of electron/ion in electrode materials. With high-temperature yttria-stabilized zirconia (YSZ) based SOFCs as an example, the well-studied NiO anode (fuel catalysis) and $La_{0.8}Sr_{0.2}MnO_3$ cathode (oxygen catalysis) both demonstrate excellent catalytic capability for reaction gas [ref?]. However, the conducting mechanism of NiO and $La_{0.8}Sr_{0.2}MnO_3$ is mainly focusing on electron-transporting properties, which restrict the three-phase boundary (TPB) zone to the narrow area of electrode/electrolyte interfaces, limiting the further improvement of power output.

To explore SOFCs with higher cell performance and lower operating temperature, it is noticed the electrode materials possess both high electron and oxygen ion conduction demonstrate higher power output [ref?]. Besides the excellent electron transportation, the coexisted oxygen-ion transport not only improves the catalytic ability for reaction gas, more importantly, also vastly expands the TPB of the electrode layer, providing more electrode-reaction sites for electrocatalysis. By extensive researches, the oxygen permeability as direct evidence demonstrates the existence of oxygen-ion conduction in cathode materials of SOFCs. For example, the oxygen permeability in $La_{0.6}Sr_{0.4}Co_{0.2}Fe_{0.8}O_3$ (LSCF) cathode reaches more than 1 mL min^{-1} cm^{-2} at 900 ^oC, which is mainly relying on

the arising oxygen vacancies for oxygen-ion conduction [ref?]. Shao et al. also demonstrates almost 2 mL min^{-1} cm^{-2} oxygen permeability at 900 ^oC in $Ba_{0.5}Sr_{0.5}Co_{0.8}Fe_{0.2}O_3$ (BSCF) cathode as almost the highest oxygen permeability ever in the ceramic-based membrane [ref?]. Thus, SOFCs collocating with high electron and oxygen ion co-conducting cathodes demonstrate excellent power output at lower operating temperatures.

Meanwhile, the electrocatalytic performances of anodes are also significantly improved in previous reports. By introducing O^{2-} conducting YSZ or CeO_2 based electrolyte into the electron-conducting NiO to form e^-/O^{2-} co-conducting composite anode is becoming one of the solutions. Huang et al. firstly reported that double perovskite-based anodes with both high e^- and O^{2-} conduction can catalyze different fuel gases, especially for carbon-based fuels (such as CH_4 et al.) [ref?]. For $BaZr_{0.1}Ce_{0.7}Y_{0.1}Yb_{0.1}O_3$ (BZCYYb) + NiO based anode, the outstanding catalytic ability, and anti-sulfur poisoning are also attributed to the co-conducting mechanism of e^-, O^{2-} and H^+ [ref?]. For both cathode and anode materials, the oxygen permeability is the direct evidence to evaluate the oxygen-ion conduction capability. Compared to the tremendous works in the oxygen permeability of cathode materials under air/O_2 in SOFCs, the anode materials working in reducing environments, however, has rarely been discussed.

To our knowledge, only limited literature focuses on the extrinsic anodic oxygen permeability by exposing anode ceramic in the semi-reducing state (the anode ceramic with one side in the air and another side in fuel gas). For example, under the air/CO gradient (CO as reducing atmosphere), the oxygen permeability of $Ce_{0.8}Sm_{0.2}O_2$-$La_{0.8}Sr_{0.2}CrO_3$ composite membrane anode was evaluated [Journal of Membrane Science 286 (2006) 22–25). Under (O_2+N_2)/(He+CH_4) atmosphere, Lin et al. studied the oxygen permeability of the $Bi_{1.5}Y_{0.3}Sm_{0.2}O_3$ membrane [Journal of Membrane Science 231 (2004) 133–146]. Chen et al. reveal the oxygen permeability of La_2NiO_4 tubular membranes under the air/(helium+CH_4) gradient [Catalysis Today 82 (2003) 151–156]. However, the semi-reducing state only partially reveals the intrinsic anodic oxygen permeability since the oxygen in air-side cannot inspire the most real anodic state. As we all know, with anode fully exposing in fuel side, the study of intrinsic anode-oxygen-permeability has pivotal practical significance for the anode design. In this work, with H_2-reduced SZMO (R-SZMO) as anode pellet, with a dense, high oxygen-ion transportation thin-film BSCF layer sintering on the R-SZMO surface as blocking layer, the intrinsic anode oxygen-permeability is firstly studied. For the BSCF/R-SZMO composite structure, the BSCF layer exposing in air is not only used to avoid the re-oxidation of R-SZMO but also to transport sufficient O^{2-} (from air) directly to R-SZMO layer. Fully exposing R-SZMO in fuel gas side, the intrinsic anode oxygen permeability is studied by calculating the obtained O^{2-} concentration from BSCF layer. Theoretical calculations confirmed the high oxygen conduction is dominated by the formation of intrinsic anion-Frenkel defect pair. Meanwhile, SZMO shows highly efficient CH_4 conversion based on the optimal electronic structure with the assistance of the electroactive O sites on (110) surfaces. At last, SZMO as SOFCs anode demonstrates high fuel catalytic ability, excellent anti-carbon deposition, and high power output when using H_2 and CH_4 as fuel gases.

2. Materials and Methods

2.1. Material synthesis

Sr_2ZnMoO_6 powders were synthesized via a sol-gel method using the starting materials including $Sr(NO_3)_2$, $C_4H_6ZnO_4 \cdot 2H_2O$ and $(NH_4)_6Mo_7O_{24} \cdot 4H_2O$. Citric acid was used as the complexing agent and the *mol* ratio with metal ions is about 2:1. Firstly, citric acid was dissolved into 250 ml distilled water, and then the chemical constituents were weighed carefully according to the stoichiometry and added successively under stirring until the formation of a clear aqueous solution. The solutions were slowly evaporated on hot plates for about 20 h to form gels. The gel was decomposed at 400 ºC for 10 h in the air-atmosphere to combust carbonaceous components. The powder was then ground in a mortar, and calcined at 800 ºC in air atmosphere for another 10 h to eliminate the organic substances. The calcined powder was reground and pressed into a pellet with about 13 mm in diameter and finally sintered at 1100 ºC for 10 h in air. The cathode material LSCF and BSCF were obtained via a sol-gel method and the final sintering temperature was carried out at 1000 ºC for 5 h in air. The fabrication of anode materials Sr_2MgMoO_6 (SMMO) and Sr_2CoMoO_6 (SCMO) are described in previous works [Huang and Tao]. The electrolyte $La_{0.9}Sr_{0.1}Ga_{0.8}Mg_{0.2}O_{3-\delta}$ (LSGM) was prepared by glycin–nitrate technique and the final sintering temperature is 1450 ºC for 10 h. The sintered ceramic disks were ground and polished until the thickness reached about 300 μm.

Testing of oxygen permeability First, for the oxygen permeability of R-SZMO anode; the R-SZMO was obtained by exposing the pristine pure phase SZMO (P-SZMO) powder in H_2 atmosphere at 800 ºC for 2 hours. A certain amount of R-SZMO powder was pressed into sheet billet, and then a thin BSCF layer was pressed onto one side of the R-SZMO sheet billet by dual dry pressing method. The complex sheet billet was sintered at 1150 ºC in the Ar atmosphere for 2 hours. The obtained complex ceramics are very dense and the interlamination between BSCF and R-SZMO is tightly bound. The thickness of BSCF layer is about in 20-30 μm and the R-SZMO layer is about in 1mm (**Figure S1**). The oxygen permeation experiments were performed in a vertical high-temperature gas permeation system. The obtained BSCF/R-SZMO complex ceramic was sealed on alumina tube with glass encapsulant. The effective inner surface area of the membrane disc was controlled around 0.85 cm^2. Dense BSCF as blocking layer was exposed to the air side to avoid the direct contact of R-SZMO with air, and then to avoid the re-oxidation of R-SZMO. During anodic oxygen permeability testing, R-SZMO layer was completely exposed into different carrier gases at a flow rate of 30 ml min^{-1} (including He, H_2, CH_4, and CO_2), and dried air at a flow rate of 150 ml min^{-1} was used as the feed gas to supply to the BSCF layer. The amount of nitrogen was used to detect the leakage. With oxygen gradient as a driving force, the oxygen ions transport from dry air to BSCF layer and then to R-SZMO layer, at last to the carrier gases. Two hours are given for each tested temperature and for each change of testing gas to reach equilibrium, and each step lasts for more than 5 hours. The oxygen permeability of R-SZMO operating in different fuel gases was calculated like this: as the oxygen permeability of BSCF is much higher than R-SZMO, the obtained results were calculated just by the thickness of R-SZMO (ignore the BSCF thickness), which was regarded as the anodic oxygen permeability of R-SZMO.

The oxygen permeation flux was calculated from the concentration of the oxygen or the oxygen-containing species and flow rate at the outlet. The oxygen permeability of BSCF and P-SZMO was tested by exposing one side to Air and another side to the different carrier gases. The O_2 flux measurement was tested by on-line micro gas chromatography (Varian 490-GC, Varian) from 600 to 900 ◦C. The sintered membranes with relative densities higher than 90% were used for oxygen permeation studies. In order to ensure the bulk oxygen ionic conductivity is predominantly limited by the oxygen migration, porous platinum as a catalyst was deposited onto the ceramic surface.

The catalytic activity of R-SZMO anode for fuel gas was evaluated in a fixed-bed quartz tubular microreactor. To minimize the effect of hot spots, the sample (20 mg, 40–60 mesh) was diluted with 0.25 g quartz sands (40–60 mesh). The volumetric composition of the reactant mixture was 10% CH_4 + 5% O_2 + 85% Ar (balance), and the total flow was 41.6 mL/min, thus giving a gas hourly space velocity (GHSV) of ca. 30,000 mL/(g h). The concentrations of the reactants and products were monitored online by a gas chromatograph (Agilent 7890A). Using a mass spectrometer (HPR20, Hiden), we detected only methane, carbon dioxide, and water in the outlet gas mixture from the microreactor. The balance of carbon throughout the investigations was estimated to be 99.5%. The relative errors for the gas concentration measurements were less than ±1.5%. The catalytic activities of the samples were evaluated using the temperatures (T65%, and T90%) required for methane conversions 65, and 90%, respectively. CH_4 conversion was defined as $(c_{inlet}-c_{outlet})/c_{inlet} \times 100\%$, where the c_{inlet} and c_{outlet} were the CH_4 concentrations of inlet and outlet feed stream, respectively. The H_2 temperature-programmed reduction (H_2-TPR) experiments were carried out on ChemBET TPR/TPO (Quantachrome, US) equipped with TCO analyzer using a 10%.vol% H_2/Ar gas flown of 60 ml min^{-1} and passed approximately over 100 mg samples. The reduction temperature was linearly raised at 10 ^oC min^{-1} from 200 to 800 ^oC.

2.2. Single fuel cell fabrication and testing condition

We fabricate the single fuel cell by an electrolyte-supported technique. The SZMO samples were tested as anode materials in SOFCs (SZMO/LSGM/LSCF) with a 300 μm thick LSGM disk as electrolyte and LSCF as the cathode. SZMO and LSCF were made into inks with a binder (10% ethylcellulose + 90% terpineol). SZMO ink was printed onto one side of the LSGM disk followed by firing at 1200 ^oC in air for 1 h. LSCF ink was subsequently printed on the other side of the LSGM disk and sintered at 1050 ^oC in air for 1 h. Ag wires with a small amount of Ag paste in separate dots were used as current collectors at both of the anode and cathode sides for ensuring contact.

The electrical conductivity of the samples was measured using a direct current four-probe method. The measurements of conductivity were carried out in air or in pure H_2 gas (50 mL min^{-1}) among the temperature ranges from 300-800 ^oC. Before measurement in H_2, the SZMO samples were reduced in H_2 at 800 ^oC for 2 h to ensure the formation of low-valence cations and more oxygen vacancies.

The phase purity and the structure parameters of the samples were checked by X-ray diffraction (XRD) with the Philips X'Pert PRO diffractometer. Thermogravimetric (TG) and differential scanning calorimetry (DSC) measurements were performed on a NETZSCH STA 449C simultaneous thermal analyzer in 5% H_2/Ar mixture gas with a flow rate of 100

mL min^{-1} from room temperature to 900 ºC at a heating rate of 10 ºC min^{-1}. The diffraction profiles were analyzed with a Rietveld refinement program. The thermal expansion coefficient (TEC) was carried out using a horizontal pushrod dilatometer (Netzsch DIL 402 C) with an Al_2O_3 reference in the temperature range from room temperature to 900 ºC at a heating rate of 5 ºC min^{-1} and 5% H_2/Ar as the purge gas. Cell power output and electrochemical impedance spectra were carried out with the IM6 platform. Scanning electron microscope (SEM; JEOL JSM-6480LV) was employed to examine the microstructures of the sintered samples. X-ray photoelectron spectroscopy (XPS) measurements were performed in a PHI 5600 (Physical Electronics) photoelectron spectrometer.

2.3 Calculation Setup

All the calculations are performed by the density functional theory (DFT) within the CASTEP codes [1]. The ultrasoft pseudopotential scheme has been chosen with the generalized gradient approximation (GGA) and Perdew-Burke-Ernzerhof (PBE) for the exchange-correlation energy, in which the 330 eV cut-off energy is applied [2-5]. For all the geometry optimizations, the Hellmann-Feynman forces will be converged to less than 0.001 eV/A while the total energy has been converged to 5×10^{-5} eV per atom. The Gamma k-point has been applied for the energy minimization based on the Broyden-Fletcher-Goldfarb-Shannon (BFGS) algorithm [6-7]. For the electrocatalysis calculations, we have cleaved (100) and (110) surfaces from SZMO unit cell to compare the electroactivity. For a full relaxation of the local lattice within adsorption, a 15 Å vacuum space along z-direction to supply sufficient space is introduced.

3. Results and discussion

In **Figure. 1a**, our selected BSCF ceramic shows excellent oxygen permeability in an air atmosphere, which means that BSCF can be used as a coating layer to transports sufficient O^{2-} ions from air to the R-SZMO side. For P-SZMO, the calculated oxygen permeability also is very high with He, CO_2 or H_2 as carrier gases. The permeation fluxes increase with the increase of temperature. P-SZMO exposing in the semi-reducing state (air/H_2), demonstrates apparently higher oxygen permeability than in air/CO_2 and air/He, which is caused by the partial reduction of P-SZMO (at the H_2 side) to R-SZMO. Switching the carrier gas from He to CO_2, the anode oxygen permeability shows a slight decrease, which is attributed to the absorption of CO_2 on SZMO surface. Furthermore, with BSCF/R-SZMO composite ceramic as oxygen separation membrane, the anodic oxygen permeability has been greatly improved as shown in **Figure 1b**. When operating at 900 ºC in air/H_2 gradient, the oxygen permeability is greatly improved from 0.089 ml cm^{-2} min^{-1} of P-SZMO to 0.84 ml cm^{-2} min^{-1} of R-SZMO, almost 10 times enhancement is achieved. With the carrier gas changes from H_2 to CH_4, He and CO_2, a gradually decreased oxygen permeability and increased activation energy are observed. More clearly, with BSCF/R-SZMO composite ceramic working at 900 ºC as an example, **Figure 1c** shows the variations of oxygen permeability affected by different carrier gases. Science fuel gases are available at the oxygen-lean side, the oxygen permeability reaches as high as 0.84 ml cm^{-2} min^{-1} and 0.76 ml cm^{-2} min^{-1} in air/H_2 and air/CH_4 gradient, which can compare with LSCF cathode.[2a, 2b] [a] B. Wang, *J. Power Sources* **2005**, 152, 1; b] H. A. Gasteiger, S. S. Kocha,

B. Sompalli, F. T. Wagner, *Appl. Catal. B Environ.* **2005**, 56, 9;]. This can be explained by from both thermodynamic and kinetic perspectives that; 1) the fuel gases (H_2 and CH_4) are reduced by porous Pt catalyst, then the permeated oxygen is coupled with the reduced fuel gases, which provides a large driving force for the oxygen permeation in terms of thermodynamics; 2) the permeated oxygen ions do not need to recombine into oxygen molecules at the oxygen-lean side; instead, they can directly react with the adsorbed fuel gas, which process is favorable in terms of kinetics. Inert He as carrier gas has no chemical reaction with permeated oxygen, herein, the anodic oxygen permeability is moderate. The oxygen permeability shows a further drop when CO_2 was used as carrier gas, which is ascribed to the absorption of CO_2 on the R-SZMO surface. After the carrier gases were switched back from CO_2 to He, CH_4 and H_2 again, oxygen permeability recovers to the original level, indicating that the material decomposition and carbonate formation due to CO_2 attack are limited to the surface area. On the other hand, the long-term stability is a crucial factor for the practical applications of oxygen permeation membranes. **Figure 1d** shows the oxygen permeability of P-SZMO and BSCF/R-SZMO membranes as a function of operation time under air/H_2(CH_4) atmosphere at 900 °C. No obvious decrease in oxygen permeation fluxes is observed during the whole operating time, which indicates that SZMO as oxygen-permeability membrane possesses excellent long-term stability.

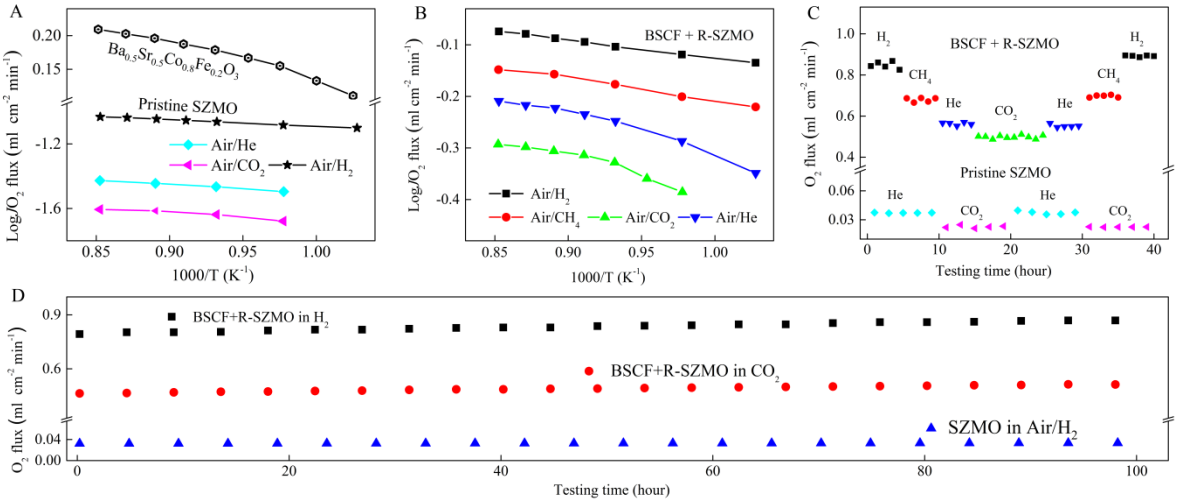

Figure 1. Anode oxygen permeability of P-SZMO and BSCF/R-SZMO with air as feeding gas and operating in different carrier gases. Anode oxygen permeability as a function of temperatures for (a) P-SZMO (BSCF for comparison) and, (b) BSCF/R-SZMO composite ceramics; (c) the variations of anode oxygen permeability for BSCF/R-SZMO under different carrier gases at 900 ºC; (d) long term stability.

The conductivity σ as a function of increasing temperature is tested to evaluate the SZMO catalytic ability and was displayed in **Figure. 2a**. In an air atmosphere, the conductivity σ for P-SZMO at 800 ºC is about 7.2 S cm^{-1}. After exposing in H_2 at 800 ºC for 2 h, R-SZMO shows an apparent conductivity increase to 30.9 S cm^{-1} at 800 ºC, which is due to the introduction of more small-polaron models in MoO_6 octahedrons after the reduction. The value of activation energy E_a is obtained by the linear fit of the conductivity plot, in which R-SZMO in H_2 (0.012 ± 0.001 eV) shows much lower activation barrier than P-SZMO in air (0.242± 0.001 eV), indicating that the electronic conduction demonstrates the predominant factor.

The methane conversion rate of R-SZMO catalyst is carried out as a function of temperature (ranging from 500 to 800 ºC) as shown in **Figure 2b**. The methane catalytic performance with La_2CuO_4 [27], $LaSrCuO_4$[27], $La_{0.6}Sr_{0.4}MnO_3$ [28] and $YBa_2Cu_3O_7$ [29] as catalysts are also listed for comparison. At 500 ºC, the R-SZMO catalyst demonstrates 65% conversion rate for methane. Notably, the methane conversion rate increases monotonously with the rise of temperature and reaches 100% at 750 ºC. Undoubtedly, the methane conversion of the R-SZMO catalyst outperforms most of the above-mentioned metal oxide catalysts at temperatures ranging from 500 ºC to 800 ºC, especially at lower temperature. In short, these results indicate that R-SZMO is a potential anode material for intermediate temperature SOFCs with methane-based fuel. Except the methane conversion rate, the H_2 oxidizing ability is another critical factor to evaluate the SOFC anode material. **Figure 2c** supplies the H_2-TPR profiles for R-SZMO anode and then the comparison with Sr_2CoMoO_6, Sr_2NiMoO_6, and $Sr_2Fe_{1.5}Mo_{0.5}O_6$ [ref?]. The first peak corresponds with the onset temperature of anode for H_2 reduction. In comparison, R-SZMO shows the first peak at the lowest temperature around 320 ºC, supporting that H_2 oxidation is facile to achieve by SZMO anode.

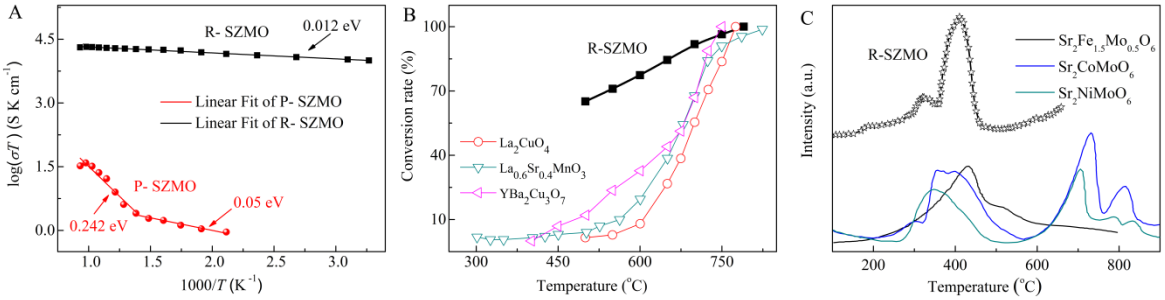

Figure 2. (a) Arrhenius plots of conductivity as a function of temperature for P-SZMO testing in air and R-SZMO testing in H_2; the comparison of R-SZMO anode with some selected catalysts about methane conversion rate (b) and hydrogen catalytic ability (c) as a function of temperatures. La_2CuO_4 [27], $LaSrCuO_4$[27], $La_{0.6}Sr_{0.4}Mno_3$ [28] and $YBa_2Cu_3O_7$ [29].

Figure. 3a shows the XRD structural refinements and the corresponding fitting results by the GSAS software package for P-SZMO and R-SZMO samples, respectively. The lattice parameters, bond lengths, and bond angles are displayed in **Table S1**. From the corresponding optical pictures in **Figure 3b**, the beige P-SZMO after hydrogen reduction shows an apparent color variation to blue-black R-SZMO. XPS measurement is carried out with P-SZMO and R-SZMO as examples to confirm the oxidation state of molybdenum elements, **Figure. 3c**. By XPS analysis, the binding energies and the valent state contributions of Mo are summarized in **Table S2**. For P-SZMO, the Mo 3d peak is fitted by using four components, two for the $3d_{3/2}$ and two for the $3d_{5/2}$, indicating the Mo^{5+} and Mo^{6+} valence state, respectively. The binding energies of P-SZMO extracted from the fitting procedure are 232.2 eV and 230.4 eV for the Mo-$3d_{5/2}$ peak and 233.5 eV and 235.4 eV for the Mo-$3d_{3/2}$ peak. These values are in good agreement with the reported values, 230 eV and 233 eV for Mo^{5+} and 232.2 eV and 235 eV for Mo^{6+} [26]. The valence-state variation of P-SZMO extracted from the fitting procedure is 6% for Mo^{5+} and 94% for Mo^{6+}. For

R-SZMO, the Mo 3d peak is fitted by six components, three for the $3d_{3/2}$ and three for the $3d_{5/2}$, indicating the Mo^{4+}, $Mo^{5+,}$ and Mo^{6+} valence state, respectively. The ion concentration in R-SZMO is 8% for Mo^{4+}, 16% for Mo^{5+} and 76% for Mo^{6+}. TG-DSC measurement in **Figure S2** also confirms the introduction of mobile bulk oxygen vacancies (by lattice oxygen loss) and the reduction of Mo(VI) to Mo(V) in the SZMO sample (exposing in 5% H_2/Ar mixture gas). By XRD structural refinement in **Figure 3d**, the mean bond length of <Mo-O> in R-SZMO is 1.892 Å, longer than that in P-SZMO (1.864 Å). The explanation is that, from P-SZMO to R-SZMO, a part of Mo^{6+} ions (0.59 Å, sixfold) were converted to Mo^{5+} (0.61 Å, sixfold) and Mo^{4+} ions (0.65 Å, sixfold) by hydrogen reduction. The bigger Mo^{5+} and Mo^{4+} ions lengthen the <Mo-O> bond.

Figure 3e shows that corner-shared MoO_6 and ZnO_6 octahedrons are neatly arranged in SZMO and build the perovskite skeleton. The ion radius of Zn^{2+} (0.74 Å) is bigger than $Mo^{6/5/4+}$, which means the volume of $ZnO_{6/2}$ is larger than $MoO_{6/2}$ octahedra. Due to the cooperative rotation and mismatched volume ratio of $ZnO_{6/2}$ with $MoO_{6/2}$ octahedra, the Zn-O-Mo bond angle is twisted. In P-SZMO, the Zn-O-Mo bond angle is about 174°. In R-SZMO, although the valence of Zn ions is still divalent, the mean bond length of <Zn-O> is shortened from P-SZMO to R-SZMO, which we think is mainly caused by the oxygen escaping (cause oxygen vacancy) after hydrogen reduction. And for the $MoO_{6/2}$ octahedra, more $Mo^{5/4+}$ ions with a bigger radius lengthened the mean <Mo-O> bond length. Herein, the shortened <Zn-O> bond and the lengthened <Mo-O> bond in R-SZMO slightly release the twisted orientation of the corner-shared MoO_6 and ZnO_6 octahedrons (Zn-O-Mo bond angle) to 177°. Although the oxygen vacancies are the key sites for lattice oxygen diffusion via the hopping mechanism, the oxygen ions transportation is controlled by the critical radius (r_c) of the opening size,[37] which was configured by two A site ions and one B site ion. Although the XRD refinement results indicate that P-SZMO and R-SZMO are both in tetragonal structure with space group I4/m (**Figure S3**), the increased Zn-O-Mo bond angle in R-SZMO corresponds with higher lattice symmetric structure (geometric tolerance factor $t = (r_A + r_O)/\sqrt{2}(r_B + r_O)$, the r_A, r_B, and r_O are the ionic radii of Sr^{2+} (twelvefold coordination), the mean B-site ionic radius (sixfold coordination), and the oxide-ion radius (eightfold coordination)[25]). R-SZMO with higher symmetric structure enlarges the critical radius r_c (opening size) by lattice relaxation, and then leaves favorable pathways for O^{2-} transportation by the hopping mechanism. Thus, the electronic and oxygen-ion conduction is analyzed in **Figure 3e**. As the valence state of Zn ions is divalent, the small-polaron model only occurs in the MoO_6 octahedrons (Mo-O-O-Mo) by the alterable oxidation state of Mo ions. In R-SZMO, more Mo(VI) was reduced to Mo(V) or Mo(IV), which provides more $Mo^{4/5+}/Mo^{6+}$ small polaron couples for electronic conduction. For O^{2-} transportation, R-SZMO with larger free space and more oxygen vacancies in the octahedral structures accelerate the lattice oxygen diffusion.

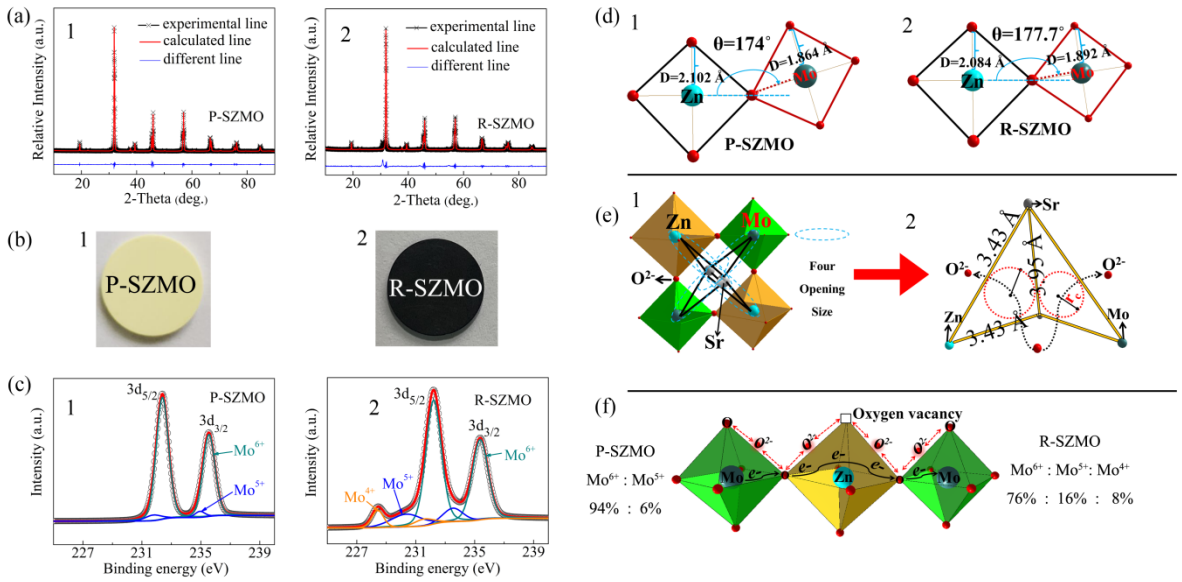

Figure 3. Physical characterization of P-SZMO and R-SZMO samples by (a) XRD structural refinement, (b) optical analysis, (c) valence state analysis by XPS spectra of Mo-3d, (d) variation of band length and band angle in MoO_6 and ZnO_6 octahedrons, (e) the critical opening size analysis and, (f) electron and oxygen ion transporting mechanism.

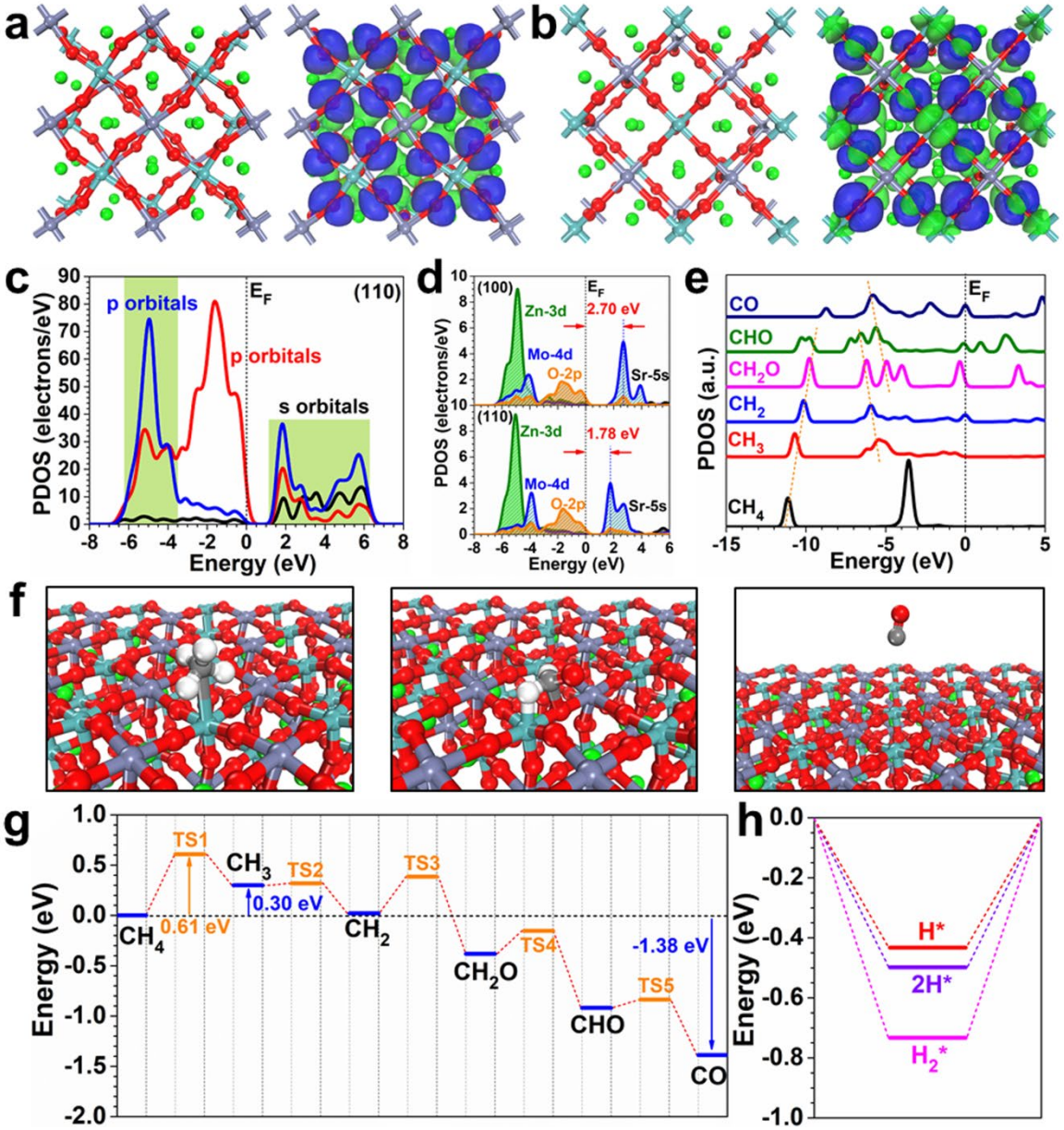

Figure 4. Theoretical calculations of the electrocatalysis for CH_4 conversion. (a) The local relaxed structure and electronic distribution near E_F of SZMO (100) surface. (b) The local relaxed structure and electronic distribution near E_F of SZMO (110) surface. Green balls = Sr; Grey balls = Zn; Cyan balls = Mo; Red balls = O (c) The PDOS of SZMO (110) surface. (d) The detailed PDOS comparison of (100) and (110) surfaces. (e) The TDOS of adsorbates during CH4 conversion on SZMO (110) surface. (f) The structural configuration of adsorbed *CH_3, *CH_2, and *CH_2O. (g) The free energy diagram of CH_4 conversion. (h) The adsorption energy of H species.

To further confirm the superior electrocatalytic performance of SZMO, we apply the density functional theory (DFT) to further explore the intrinsic mechanism especially for CH_4 reformation reactions. The distinct electronic distributions of the (100) and (110) surfaces of SZMO are illustrated. Notably, the bonding and anti-bonding distribution near the Fermi level (E_F) in (110) surfaces show stronger mixing electronic distribution with the electron-rich feature on the surface (**Figure 5a and 5b**). The PDOS of the detailed orbital

contribution on (110) surface indicates that O-2p bands substantially dominate the CBM. Meanwhile, the VBM shows *s-p-d* hybrid orbital contributions (**Figure 5c**). The more specific orbital contribution also shown that the gap for electronic transfer on the surface is alleviated from 2.70 eV in (100) surfaces to 1.78 eV in (110) surface, supporting the higher electroactivity of (110) surface **(Figure 5d)**. Thus, the (110) surfaces are selected to investigate the CH_4 conversion catalysis in SOFC. With the continuous dehydrogenation proceeds [3], the *s*-orbital presents a linear trend, indicating a substantial efficiency of electron-transfer and high selectivity towards the conversion to CO. In particular, this linear correlation is well preserved even with the adoption of O towards the adsorbates, supporting the high electroactivity for CH_4 reformation process **(Figure 5e)**. From local structure perspectives, the optimized adsorption of key intermediates CH_3, CH_2 and CH_2O all locate near the Mo and O sites **(Figure 5f)**. From the energetic perspective, the CH_4 conversion to CO only shows a slight energy barrier of 0.30 eV at the initial activation of CH_4, which also displays the highest activation energy of 0.61 eV. Afterwards, the electrocatalysis process exhibits a downhill trend with -1.38 eV energy releasements, supporting the superior performance of the CH_4 conversion **(Figure 5g)**. In addition, the adsorption energies of H-species demonstrate a spontaneous reaction from $H^*+H^* \rightarrow 2H^* \rightarrow H_2$, which further boost up the overall CH_4 reformation **(Figure 5h)**. Therefore, the superior electrocatalytic performance of SZMO is confirmed by both electronic and energetic calculation results.

In order to study the catalytic activity of SZMO anode for fuel gases, especially for carbon-based fuel gases, **Figure 5a** is the summary of the polarization resistance and long term durability of SZMO by comparing with other anodes exposing in the CH_4 atmosphere at 800 ^oC. The inset is the electrochemical impedance spectra of R-SZMO anode determined using symmetrical cells immersed in CH_4 as a function of testing time. Clearly, the impedance of the Ni+SDC electrode increased significantly with time while no apparent degree of degradation increased for SZMO and SMMO anode materials. Moreover, the impedance of SZMO displays the lowest polarization and excellent stability under the same testing conditions. SMMO remains relatively constant, but at the original polarization resistances is much higher than the SZMO electrodes. The low anode polarization for SZMO is attributed to the high anodic oxygen permeability and excellent methane catalytic ability. As shown in **Figure 5b**, the Raman spectra of the SZMO are featureless without any observable peaks when operating at 500 ^oC and exposing in CH_4, indicating that SZMO is inactive for the carbon deposition. Raman measurement results clearly confirm that the SZMO surface is much more robust against carbon formation than the Ni anode surface.

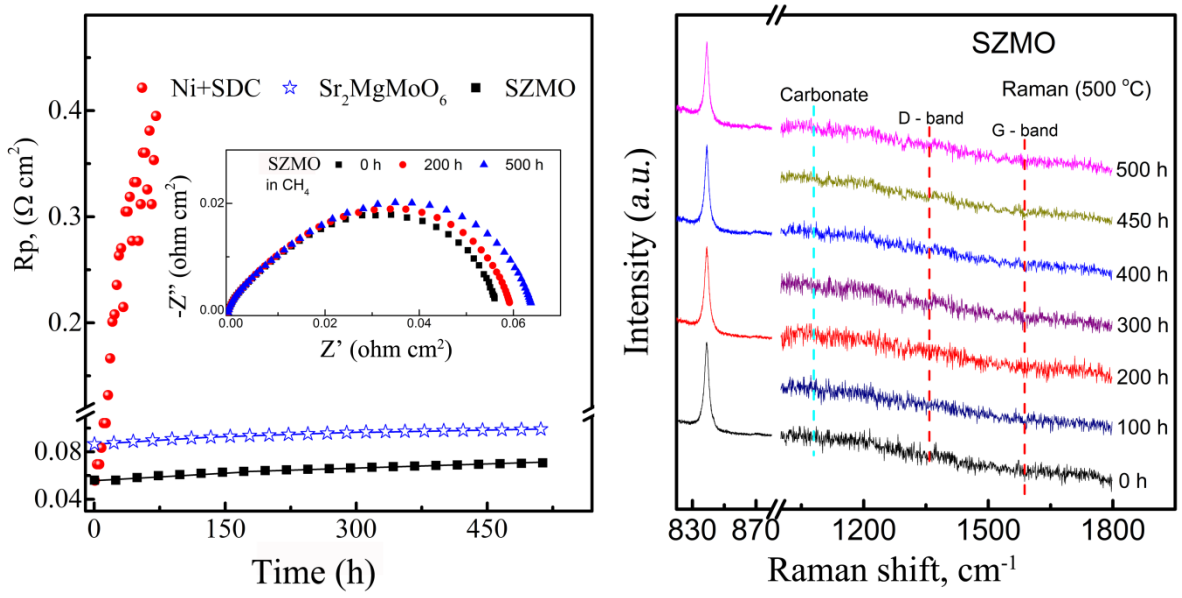

Figure 5. (a) Comparison of anode polarization durability of SZMO with Ni+SDC and SMMO anodes in the CH_4 atmosphere under OCV conditions. Insets are the EIS of SZMO, and (b) In situ surface-enhanced Raman spectroscopic (SERS) study of the R-SZMO anode in CH_4 atmosphere and operating at 500 ºC.

Although the electrolyte-supported single-cell cannot fully reveal the optimal performance due to its high ohmic drop, it is still useful to compare the catalytic ability of different anode materials. With 300 μm thick LSGM electrolyte as supporting substrate and with H_2 and CH_4 as fuel gases, the voltage, power density and long-term stability of the single-cell are shown in **Figure 6**, respectively. With hydrogen as fuel gas, SZMO anode demonstrates 570 mW cm^{-2} power densities at 800 ºC, which is comparable with most of the well-studied oxide-based anode materials (**Figure 6a**). From our work, with CH_4 as fuel gas, SZMO anode demonstrates the highest power output (330 mW cm^{-2} at 800 ºC) when compared with some of the other well-studied oxide-based anode materials (**Figure 6b**). In order to evaluate the stability of SZMO anode, the single-cell long-term stabilities were consecutively carried out for 110 h with H_2 and CH_4 as fuel gases (**Figure 6c**). No obvious degradations are found in the power density, indicating high stability when SZMO as the anode in SOFCs. The electrochemical impedance spectra (EIS) of half-cell and full-cell with SZMO as the anode are operated at different temperatures under open-circuit conditions (**Figure S4**). From the exploded view, the total resistance (R_{total}) for half-cell is mainly derived from the ohmic resistance (R_{ohm}) and the polarization resistance (R_p) is responsible for the full cell. Herein, the SZMO anodic polarization is unlikely the source for high R_p, which mainly derived from the oxygen reduction and oxygen-ion transportation through the cathode/electrolyte interface ($R_{p\ cathode}$). As shown in **Figure S5**, the SEM images of SZMO anode present the cross-section of SZMO/LSGM/LSCF configuration and the LSGM/SZMO interface. The interfaces between the electrolyte and SZMO are clear, indicating the excellent chemical stability and thermal structural matching. The dilatometric curves of SZMO are shown in **Figure S6**, in which the almost straight line of $\Delta L/L_0$ confirms that SZMO is very stable with no apparent phase transition in SOFCs. The average thermal expansion

coefficient (TEC) from room temperature to 900 °C is about 15.7×10^{-6} K^{-1}, which is only slightly higher than that of LSGM (12.3×10^{-6} K^{-1}), demonstrating good thermal compatibility with IT SOFCs electrolytes.

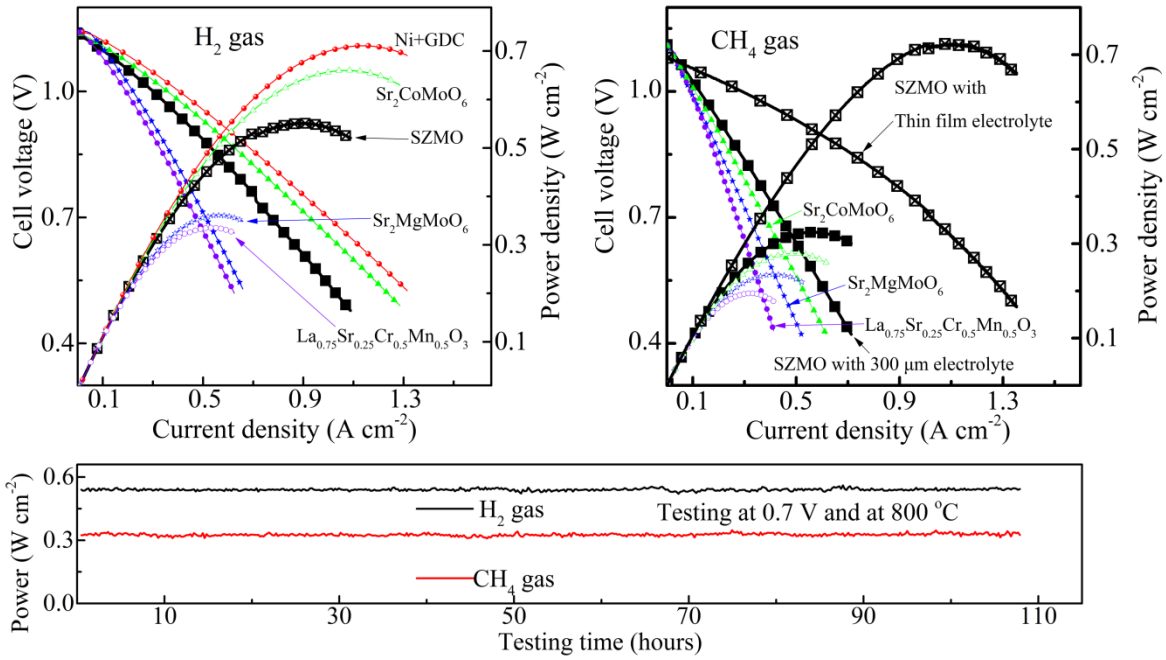

Figure 6. Single-cell power densities as a function of current density for SZMO anodic material working in (a) H_2 and (b) CH_4 fuel gas, and the comparison with other selected anode materials, and (c) the long-term stability operating at 0.7 V and 800 °C.

4. Conclusion

In summary, by a proposed coating layer structure, this work firstly evaluated the intrinsic anodic oxygen permeability by exposing of the anode in fuel gas atmosphere. We demonstrate that SZMO as a future potential anode candidate with excellent oxygen permeability and efficient fuel catalytic activity for fuutre inter-mediate SOFC with flexible carrier gases. SZMO exhibits the high electroactivity based on the optimal electronic structure with the assistance of the electroactive O sites along the CH_4 conversion process. Energetic calculations support the low energy barrier for both CH_4 conversion, supporting the highly efficient CH_4 conversion in experiments. In addition, we have demonstrated that the methane conversion rate on the SZMO catalyst is triggered by the high oxygen permeability, resulting in the excellent power output and anti-carbon deposition capability. This work presents the new insight about the intrinsic anode oxygen permeability, which opens new possibilities for evaluating highly active anodic catalysts with advanced and effective strategy based on the O^{2-} transporting capability.

Reference:

[1] S. J. Clark; M. D. Segall; C. J. Pickard; P. J. Hasnip; M. J. Probert; K. Refson; M. C. Payne, First Principles Methods Using Castep. *Zeitschrift Fur Kristallographie* **2005,** *220* (5-6), 567-570.

[2] D. Vanderbilt, Soft Self-Consistent Pseudopotentials in a Generalized Eigenvalue Formalism. *Physical Review B* **1990,** *41* (11), 7892-7895.

[3] J. P. Perdew; K. Burke; M. Ernzerhof, Generalized Gradient Approximation Made Simple. *Phys Rev Lett* **1996,** *77* (18), 3865-3868.
[4] P. J. Hasnip; C. J. Pickard, Electronic Energy Minimisation with Ultrasoft Pseudopotentials. *Comput Phys Commun* **2006,** *174* (1), 24-29.
[5] J. P. Perdew; J. A. Chevary; S. H. Vosko; K. A. Jackson; M. R. Pederson; D. J. Singh; C. Fiolhais, Atoms, Molecules, Solids, and Surfaces: Applications of the Generalized Gradient Approximation for Exchange and Correlation. *Physical Review B* **1992,** *46* (11), 6671-6687.
[6] J. D. Head; M. C. Zerner, A Broyden—Fletcher—Goldfarb—Shanno Optimization Procedure for Molecular Geometries. *Chem Phys Lett* **1985,** *122* (3), 264-270.
[7] M. I. J. Probert; M. C. Payne, Improving the Convergence of Defect Calculations in Supercells: Anab Initiostudy of the Neutral Silicon Vacancy. *Physical Review B* **2003,** *67* (7).